
This is an electronic reprint of the original article.
This reprint may differ from the original in pagination and typographic detail.

Shah, M. A.K.Yousaf; Lu, Yuzheng; Mushtaq, Naveed; Rauf, Sajid; Yousaf, Muhammad; Asghar, Muhammad Imran; Lund, Peter D.; Zhu, Bin

Demonstrating the potential of iron-doped strontium titanate electrolyte with high-performance for low temperature ceramic fuel cells

Published in:
Renewable Energy

DOI:
[10.1016/j.renene.2022.06.154](https://doi.org/10.1016/j.renene.2022.06.154)

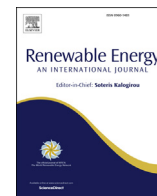
Published: 01/08/2022

Document Version
Publisher's PDF, also known as Version of record

Published under the following license:
CC BY

Please cite the original version:
Shah, M. A. K. Y., Lu, Y., Mushtaq, N., Rauf, S., Yousaf, M., Asghar, M. I., Lund, P. D., & Zhu, B. (2022). Demonstrating the potential of iron-doped strontium titanate electrolyte with high-performance for low temperature ceramic fuel cells. *Renewable Energy*, 196, 901-911. <https://doi.org/10.1016/j.renene.2022.06.154>

This material is protected by copyright and other intellectual property rights, and duplication or sale of all or part of any of the repository collections is not permitted, except that material may be duplicated by you for your research use or educational purposes in electronic or print form. You must obtain permission for any other use. Electronic or print copies may not be offered, whether for sale or otherwise to anyone who is not an authorised user.



Demonstrating the potential of iron-doped strontium titanate electrolyte with high-performance for low temperature ceramic fuel cells



M.A.K. Yousaf Shah^a, Yuzheng Lu^{b, **}, Naveed Mushtaq^a, Sajid Rauf^c,
Muhammad Yousaf^a, Muhammad Imran Asghar^{d, e, *}, Peter D. Lund^{a, d}, Bin Zhu^{a, ***}

^a Jiangsu Provincial Key Laboratory of Solar Energy Science and Technology/Energy Storage Joint Research Center, School of Energy and Environment, Southeast University, No.2 Si Pai Lou, Nanjing, 210096, China

^b School of Electronic Engineering, Nanjing Xiaozhuang University, 211171, Nanjing, China

^c College of Electronics and Information Engineering, Shenzhen University, Guangdong Province, 518000, China

^d New Energy Technologies Group, Department of Applied Physics, Aalto University School of Science, P. O. Box 15100, FI-00076, Aalto, Espoo, Finland

^e Faculty of Physics and Electronic Science, Hubei University, Wuhan, Hubei, 430062, China

ARTICLE INFO

Article history:

Received 3 January 2022

Received in revised form

26 May 2022

Accepted 30 June 2022

Available online 14 July 2022

Keywords:

Ceramic fuel cell (CFC)

Electrolyte

Proton conducting

Schottky junction

Higher fuel cell performance

ABSTRACT

Electrolytes with high-proton conduction and low activation energy are attractive for reducing the high operating temperature of solid-oxide fuel cells to less than <600 °C. In this work, we have fabricated semiconducting electrolyte SrFeTiO_{3-δ} (SFT) material exhibiting high ionic conduction and exceptionally high protonic conduction at low operating temperature but with low electronic conduction to evade the short-circuiting issue. The prepared fuel cell device exhibited high open-circuit voltage (OCV) and a high-power output of 534 mW/cm², of which 474 mW/cm² could be for sure be related to the protonic part. The current study suggests that usage of semiconductor SrFeTiO_{3-δ} facilitates a high concentration of oxygen vacancies on the surface of SFT, which mainly benefits proton conduction. Moreover, lower grain boundary resistance leads to obtain higher performance. Also, the Schottky junction phenomena are proposed to inhibit the e-conduction and excel the ions transportation. The high performance and ionic conductivity suggest that SFT could be a promising electrolyte for protonic ceramic fuel cells.

© 2022 The Authors. Published by Elsevier Ltd. This is an open access article under the CC BY license (<http://creativecommons.org/licenses/by/4.0/>).

1. Introduction

Ceramic fuel cells possess numerous attractive advantages such as fuel flexibility (hydrocarbon, hydrogen, ammonia, etc.), high efficiency, and no need for precious-metal catalysts [1–3]. In contrast, traditional SOFC fuel cells with yttria-stabilized zirconia (YSZ) electrolyte operates at high temperatures (800°–1000 °C), resulting in materials issues and high cost [4,5]. New oxygen ion-conducting electrolytes like samarium-doped ceria (SDC) or gadolinium, also known as a second-generation SOFC [5,6], enable lower

operating temperatures to ~ 600 °C. The third-generation SOFC based on nanostructured rare earth elements (including Eu or Ru and ultrathin multilayer or nanofiber heterostructure electrolytes) has reached impressive fuel cell performance at a lower temperature (450°–600 °C) [7,8]. However, decreasing the temperature, the performance drops rapidly due to the high activation energy (E_a) accompanied by oxygen-ion conduction. In comparison to oxide ion conduction, protonic conduction in oxides typically has lower E_a (activation energy), meaning that protonic ceramic fuel cells (PCFCs) hold the extensive potential to gain high fuel cell performance at low temperatures (LT) [9–13].

Past efforts in proton-conducting fuel cells include the demonstration of a stable proton conductor yttrium-doped barium zirconate (BZY), showing high (bulk) proton conductivity [14,15]. However, this material system has offered a high grain boundary resistance that has constrained its application. To overcome these problems, the semiconductor-based ceramic fuel cell has been introduced. Recently a new semiconductor perovskite material

* Corresponding author. New Energy Technologies Group, Department of Applied Physics, Aalto University School of Science, P. O. Box 15100, FI-00076, Aalto, Espoo, Finland.

** Corresponding author.

*** Corresponding author.

E-mail addresses: mrlyuzheng@163.com (Y. Lu), imran.asghar@aalto.fi (M.I. Asghar), zhu-bin@seu.edu.cn (B. Zhu).

(proton conductor), SmNiO_3 (SNO), with high ionic & electronic conductivity, was introduced, which can be exploited as an electrolyte in a low-temperature fuel cell delivering a meaningful power-density of 225 mW/cm^2 at $500 \text{ }^\circ\text{C}$, but also a high open-circuit voltage (OCV) of 1.03 V [16]. The filling-controlled Mott-transition phenomena were exploited to suppress the electronic conductivity through the SNO electrolyte. Also, SNO has shown a high H^+ conductivity at a low operating temperature of $300\text{--}500 \text{ }^\circ\text{C}$, which is among the best performing solid perovskite electrolytes [16]. Zhu et al. have presented a new idea of proton confined transportation via proton shuttles phenomena based on core-shell heterostructure using $\text{CeO}_2/\text{CeO}_{2-\delta}$ electrolyte to enhance the proton conduction up to 0.16 S/cm reaching high fuel cell performance of 697 mW/cm^2 at $520 \text{ }^\circ\text{C}$ [17]. The high concentration of oxygen vacancies on the surface layer and depletion region created by the core-shell structure at the interface confines the proton transport at the surface layer of ceria [17]. These exciting studies reveal that compared to conventional SOFC, the semiconductor-based perovskite oxides involving H^+ conduction hold more potential as an electrolyte at lower temperatures ($350\text{--}550 \text{ }^\circ\text{C}$). These results suggest that H^+ conduction in semiconductor perovskite oxides has lower activation energy than the O^{2-} due to the minimal ionic radius, and smaller mass of protons.

Undoubtedly, proton-conducting perovskite electrolytes have the advantage of enabling low operating temperatures. However, unfortunately, they face a crucial challenge of high grain boundary resistance, which leads to low ionic conductivity [18–20]. A representative proton conductor, doped barium cerate ($\text{BaCe}_{1-x}\text{M}_x\text{O}_{3-\delta}$), has low proton conductivity of $10^{-2} \text{ S cm}^{-1}$ at $600 \text{ }^\circ\text{C}$ [21]. Much effort has been devoted to developing perovskite electrolytes with high proton conduction via advanced thin-film techniques. However, the performance of PCFC still lags far behind SOFC performance. Nevertheless, from this perspective point, several proton conductors such as BZY and BCFZY enable higher performance at low temperatures. Moreover, perovskites with semiconducting properties are of increasing interest as semiconductor materials have been employed as electrolyte-membranes for LT-SOFCs [16,17,22]. Utilizing the above-stated benefits to design semiconductor-based high ion-conducting electrolytes, especially the perovskite oxides, could be a high potential for practical use in LT-SOFCs.

To obtain the high proton conduction and low activation energy, we develop the semiconductor perovskite into a proton-conducting electrolyte for LT-SOFCs. We have designed a promising perovskite SFT of p-type semiconductor, sandwiched between two $\text{Ni}_{0.8}\text{Ce}_{0.05}\text{Al}_{0.05}\text{LiO}_{2-\delta}$ (NCAL) electrodes to construct a fuel cell device. The developed SFT semiconductor-based device delivered a notable ionic conductivity and fuel cell performance at $420\text{--}520 \text{ }^\circ\text{C}$. The Schottky junction helps suppress the electronic conductivity and promote the ionic conductivity in the material. The experiments reveal that SFT can be a promising electrolyte material with dominant proton conduction for LT-SOFCs.

2. Materials and method

2.1. Powder synthesis

The sol-gel method was used to synthesize $\text{SrFe}_{0.3}\text{Ti}_{0.7}\text{O}_3$ (SFT) powders. In detail, the $\text{Sr}(\text{NO}_3)_2$, $\text{Fe}(\text{NO}_3)_3 \cdot 6\text{H}_2\text{O}$, $\text{Ti}(\text{NO}_3)_2$ (followed by mixing an appropriate ratio of TiO_2 (Sigma 99.9%) in HNO_3 – 66% purity), $\text{C}_6\text{H}_8\text{O}_7 \cdot \text{H}_2\text{O}$ and $\text{C}_{10}\text{H}_{16}\text{N}_2\text{O}_8$ (Sigma Aldrich, 99.5%) were chosen in the synthesis as a precursor. Briefly, at first, all the precursors of nitrates with a stoichiometric ratio were liquefied in EDTA (ethylene diamine tetra-acetic acid) followed by continuous heating and stirring where $\text{Fe}(\text{NO}_3)_3 \cdot 6\text{H}_2\text{O}$ was doped using surface doping technique. Then, the molar ratio of metal cation: citric acid:

EDTA = 1: 1.5: 1 was selected by adding $\text{C}_6\text{H}_8\text{O}_7 \cdot \text{H}_2\text{O}$ and $\text{C}_{10}\text{H}_{16}\text{N}_2\text{O}_8$ to the desired solution. Afterward, to adjust the pH to approximately 9, the $\text{NH}_3 \cdot \text{H}_2\text{O}$ (Sigma Aldrich) was familiarized with the solution to make it transparent. After that, the prepared solution was stirred and heated for 5–6 h to dry the water and obtain the grey gel. After that, the obtained gels were sintered at $700 \text{ }^\circ\text{C}$ in the air for 3 h and then adequately grounded to get the powder of the SFT sample. Moreover, BZY was synthesized using the sol-gel technique; the previous report discussed the detail [23].

2.2. Fuel cell construction

The NCAL electrodes' slurry was prepared using the mixture of NCAL powders and terpeneol-solvent to get a viscous liquid (slurry). The prepared thick slurry was pasted on Ni foam with a brush, then desiccated at $150 \text{ }^\circ\text{C}$ for 0.5 h to shape the Ni-NCAL electrodes. A dry pressing procedure was exploited to fabricate the SOFCs cell based on SFT electrolyte by squeezing the SFT electrolyte powder between two symmetrical Ni-NCAL ($\text{Ni-Ni}_{0.8}\text{Co}_{0.15}\text{Al}_{0.05}\text{LiO}_{2-\delta}$) (anode & cathode) electrodes into one pellet under an applied pressure of 250 MPa. Furthermore, the Ag paste was poured or pasted on the surface of electrodes to function as a current collector. The symmetrical (NCAL-Ni/SFT/NCAL-Ni) SOFC device has an active area of 0.64 cm^2 , and a thickness of 1.5 mm, while the electrolyte thickness was $750 \text{ }\mu\text{m}$. The two blocking layers of $\text{BaZr}_{0.9}\text{Y}_{0.1}\text{O}_{3-\delta}$ (BZY) O^{2-}/e^- were combined with the electrolyte layer of SFT to compile tri-layer electrolyte BZY/SFT/BZY. Then trilayers were crammed among two symmetrical electrodes (Ni-NCAL) to fabricate the five-layer device cell in the architecture of NCAL-Ni/BZY/SFT/BZY/NCAL-Ni. In the five-layer device, the thickness of the electrolyte was $450 \text{ }\mu\text{m}$ while the thickness of BZY was $130 \text{ }\mu\text{m}$. Later, online sintering was done at $600 \text{ }^\circ\text{C}$ for 0.5 h for each pellet before performance measurement.

2.3. Material characterization

The crystal structure of SFT was examined using the advanced X-ray diffractometer (XRD Bruker D8) with $\text{Cu K}\alpha$ ($\lambda = 1.54060 \text{ \AA}$), where the tube voltage was set to 45 kV and tube current to 40 mA for a reliable result. The 2θ range $20\text{--}80^\circ$ was chosen with an interval of 0.02° to collect the diffraction pattern of SFT material. Field emission scanning electron microscopy (JEOL JSM7100F field, Germany) was employed to examine the morphology of the SFT particles and the element's distribution or presence in the SFT lattice. Further, the transmission electron microscope (TEM, JEOL JEM-2100F, accelerating voltage of 200 kV) was performed to investigate the prepared specimen's microstructure. TEM-EDX with line scanning was also used to determine the composition of each element of the SFT lattice. XPS (X-ray photoelectron spectroscopy) was used to study the surface features of the SFT lattice.

2.4. Electrochemical measurements

The electrochemical-impedance-spectra (EIS) technique was implemented (Gamry, 3000 Instruments, USA) to study the (electrical and electrochemical) properties of the equipped pellet. The $0.1 \text{ Hz} - 1 \text{ MHz}$ frequency range and AC voltage signal of 10 mV were set for data collection in open-circuit voltage (OCV) mode for EIS measurements. The prepared fuel cell's current-voltage (I–V) characteristics were operated and measured under dry hydrogen and air ($120\text{--}150 \text{ mL min}^{-1}$) at $370\text{--}520 \text{ }^\circ\text{C}$. The IT8511 electronic load (ITECH Electrical Co., Ltd., China) was used to examine the measurement. However, the IT7000 software recorded the data with a scan speed of 0.02 A s^{-1} in the current-voltage sweep.

3. Result and discussion

3.1. X-ray diffraction and morphology analysis

The x-ray diffraction pattern of semiconductor perovskite SrFeTiO_{3-δ} (SFT) prevailed by performing x-ray diffraction, as shown in Fig. 1(a). The obtained diffraction peaks of SFT semiconductor are listed or well-matched with cubic perovskite structure. No prominent impurity peak has been observed due to Fe doping into STO, signifying pure cubic structure as advertised in Fig. 1(a). A little distortion appears, which might be due to low-temperature sintering for a short time. All the prevailed peaks have been assigned a hkl value of (012), (110), (111), (210), (211), (220), and (310) resembling pure perovskite structure with JPCD # 330677, with the space group of Pm3m also these peaks are as pre-reported literature [24,25]. The cubic phase can play a crucial role in producing more oxygen vacancies [26]. According to previous reports, Fe doping causes a peak shifting towards the lower angle, suggesting that Fe is well incorporated [24]. Moreover, Fig. 1(b) shows the side view of the cubic SFT lattice.

In comparing previously reported literature, the intended lattice parameter was evaluated using the Scherrer formula $D = K\lambda/L(\cos\theta)$ is 3.89605 Å, which is higher than the published literature signifying that the lattice parameter increased by surface doping of Fe. According to the Vegards Law, the enhanced lattice parameter is owed to the variance in the ionic radius of Ti and Fe [24].

Fig. 1(c and d) reveals the morphology of SFT with a magnification scale of 1 μm. Fig. 1(c) shows that the particle in the shape of a ball and iron is distributed coherently on the surface. Also, Fig. 1(d) depicts the homogeneous distribution of all particles in the SFT lattice. However, the particle size is in the nano range, leading to a large surface area with more active sites favoring the electrochemical performance. Despite particle size in the nano-size range or micro-size range, core-shell type structures in the shape of the ball have been noticed as shown in Fig. 1(c). Also, all particles are well connected, compacted, and consistently scattered, as displayed in SEM images. Homogeneity and consistency of the particles are essential parameters that make them more favorable for the speedy passage of charge carriers in the electrochemical reaction [27].

Additionally, our work mainly depends on the construction of the single-phase structure. Therefore, the core-shell structure might support ionic transport, especially ions at the surface [17]. Fig. 1(e–j) shows the EDS image of the SFT lattice, signifying that all particles are unvaryingly scattered, and Fe is well incorporated into the STO lattice as confirmed in the images.

Moreover, for a deep investigation of the morphology of SFT lattice, the HR-TEM analysis was performed supported by the EDS and line scanning. The TEM images confirm that particles are in the nano-range 50–200 nm, as displayed in Fig. 2(a and b). The atomic d-spacings of 0.276 nm are well-suited to (110) planes of cubic-perovskite SFT [24]. The amorphous phase has been noticed in TEM images, confirming the presence of core-shell structure, displayed in Fig. 2 (a, b). A core-shell structure can also help form a network of charge transport channels in the SFT lattice. The amorphous phase helps in the easy transportation of charges [17]. Moreover, separate image of SEM and HR-TEM have been displayed in the Supplementary information (Fig S11(a–d)). TEM-supported EDS mapping (Fig. 2(f–i)) approves the uniform dispersions of Sr, Fe, Ti, and O elements in the SFT lattice. Line-scanning (Fig. 2(e)) demonstrates the composition ratio of each lattice component. It is suitable to be distinguished through the physical characterization of TEM supported by EDS. The contribution of all elements including Sr, Fe, Ti, and O can be confirmed in the mapping region of the SFT lattice as shown in Fig. 2(d).

3.2. Impedance spectroscopy analysis and ionic conductivity

EIS spectra were performed to investigate the electrical properties of SFT as a frequency function in different operating temperature, as displayed in Fig. 3(a–c). The H₂/Air environment was supplied to acquire the EIS results at 420–520 °C. The EIS curve of SFT shows a spot of predominant process in the real Z-axis are witnessed for the presence of high frequency, which further intersects arc at a middle frequency and function at low-frequency range. The curve at HF, middle frequency, and lower frequency corresponds to the ohmic behavior, charge transfer and mass transfer resistance. The equivalent circuit model LR₀ (R₁Q₁) (R₂Q₂) was fitted to simulate each electrochemical process, where R₀ corresponds to ohmic resistance while R₁ and R₂ to the charge transfer (grain-boundary resistance) and mass transfer process (electrode resistance) respectively. All simulated values of EIS are displayed in Table 1. From the EIS results in Fig. 3(a), it is clear that the ohmic and grain boundary tends to decrease with increasing temperature, signifying the quick transport of charges leads to enhanced ionic conduction.

Moreover, polarization resistance exhibiting small values led to the high reaction activity of electrodes. High electrode activity must be due to the functionality of SFT as a cathode which might contribute to the interface region of electrolyte/electrode, causing high ORR (oxygen reduction reaction) kinetics at the SFT/NCAL interface [28]. Fig. 3 (b) shows the EIS analysis of a blocking-layer device of (Ni/NCAL/BZY/SFT/BZY/NCAL/Ni) structure under the H₂/air environment at different temperatures 420–520 °C. The simulated data suggest that the ohmic and polarization resistance favors the prepared device. Still, without blocking, layer cell (Ni/NCAL/SFT/NCAL/Ni) shows lower values in ohmic resistance and grain boundary resistance. This difference in resistance appears due to an additional layer of BZY (causing enhanced polarization resistance) in the cell, which causes a loss in power [29].

Furthermore, we perform the EIS analysis of SFT using a new cell under the environment of Ar (95%) and 5% of H₂ at different operational temperatures 420–520 °C, as shown in Fig. 3(c). The EIS curves at each temperature reveal the same trend as the earlier results. It can be seen that providing a purely H₂ environment shows lower ohmic and grain boundary resistance, signifying the significant contribution of protons in the prepared electrolyte SFT. All parameters obtained from ZSIMPWIN have been displayed in Table 1. EIS results using the five-layer device and employing the Ar (95%) and 5% of H₂ gases under different operational temperatures 520–420 °C have indicated the proton transportation in the SFT lattice. Therefore, proton transport in the prepared SFT electrolyte might be the dominant contributor to the ionic transport and performance output. The detailed EIS results for each device have been presented separately in supplementary information under different environments and temperatures of 520–420 °C (Fig S12–4(a–c)).

The EIS resistance was used to elucidate the total conductivity of prepared electrolyte SFT at different temperatures of 420–520 °C. The obtained total conductivity lies in the range of 0.13–0.24 S/cm at different temperatures of 420–520 °C, as demonstrated in Fig. 3(d). In addition, ionic conductivity is calculated from the I–V curve of the ohmic polarization region. The central and linear part of the I–V curve replicates the ohmic polarization resistance of the fuel cell [29]. Such as, the NCAL plays a significant role as an electrode in maintaining high electrode kinetics, so a large part of ohmic-polarization is omitted through an electrolyte membrane as an ionic conductor. The obtained resistance of SFT from the I–V curve was used to calculate the ionic conductivity via $\sigma = L/R \times A$, where L reflects the thickness of the electrolyte membrane, R is the resistance, while A is the active cross-sectional area of the

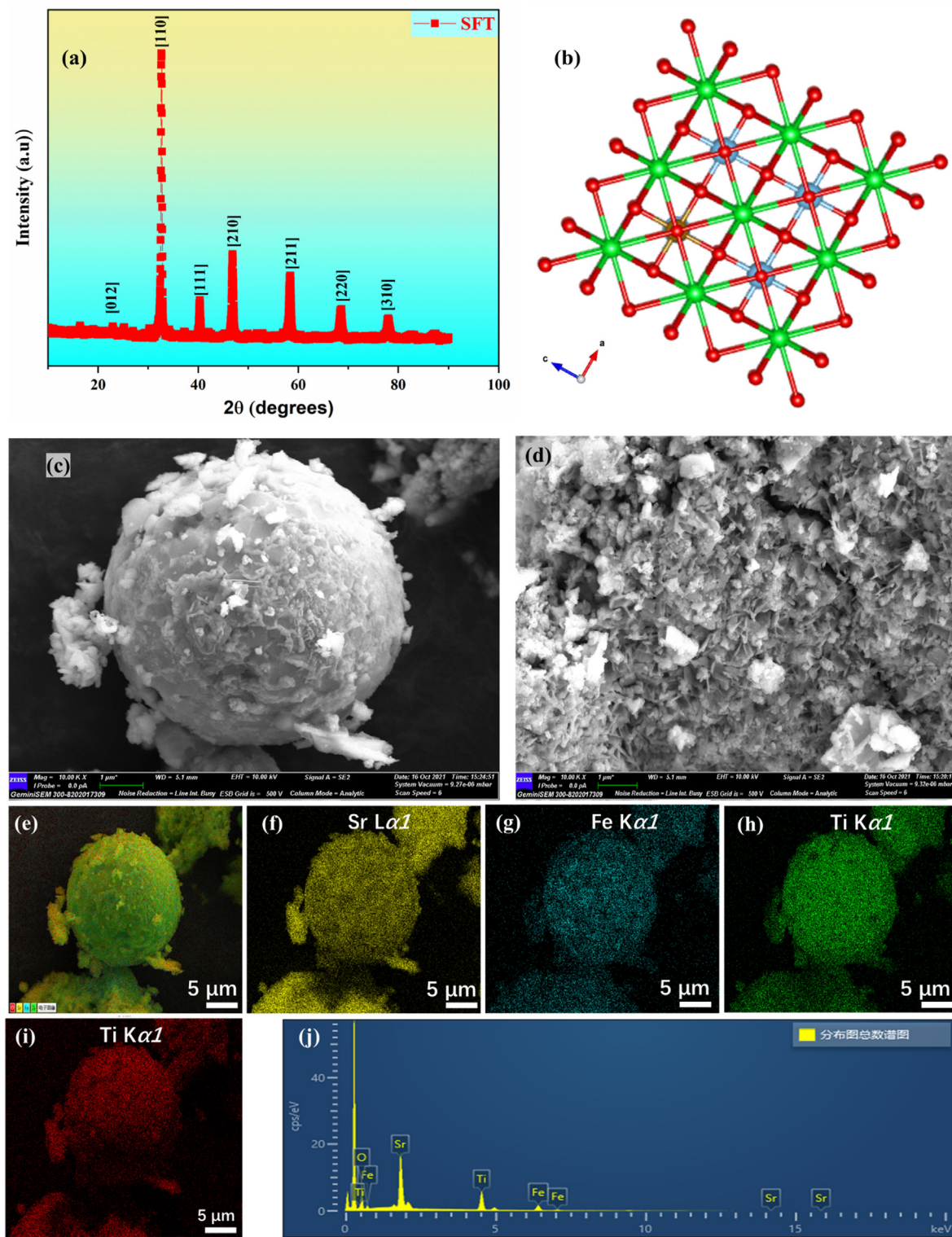


Fig. 1. (a–d) The XRD analysis of SFT, the crystal structure of SFT with (a–c) plane and SEM images of SFT at 1 μm scale while (e–j) shows the EDX images of all elements including Sr, Fe, Ti, and O.

pellet. The attained ionic conductivity of 0.18 S/cm at 520 °C is probably higher than the several reported semiconductor membranes [30].

Moreover, the obtained proton conductivity using the I–V curve from the I–V curve of the five-layer device was 0.14 S/cm

suggesting that protons' contribution is much more dominant than the oxide ions, as demonstrated in Fig. 3(d). The Arrhenius relation $\sigma T = A \exp[-E_a/(kT)]$ was implemented to elucidate the activation energy of 0.72 eV for SFT electrolyte. The obtained activation energy of SFT is lower than the reported proton conducting fuel cell

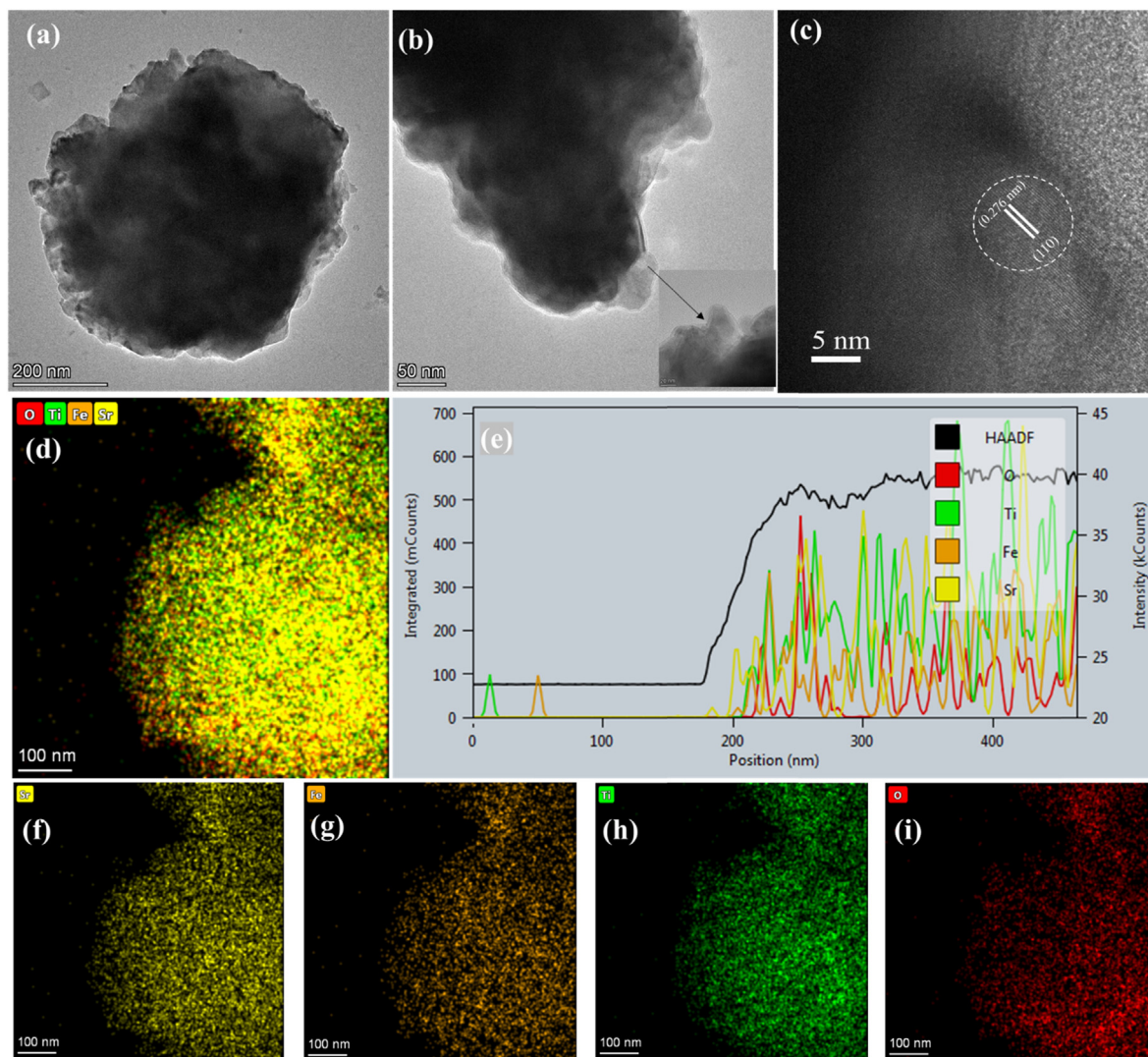


Fig. 2. (a–c) SEM images of particle distribution and multi-fringes at 110 planes while (d–i) reveals the TEM-EDX image of all elements, line scanning via EDS supported by TEM (d) mapping region, (e) line scanning, and (f–i) EDX of Sr, Fe, Ti, and O.

Table 1

The EIS data of SFT (b) BZY-SFT-BZY under H₂/Air environment while SFT under H₂ and 5% H₂ 95%Ar at different operational temperature 420–520 °C.

SFT under H ₂ /Air	R ₀ (Ω-cm ²)	R ₁ (Ω-cm ²)	R ₂ (Ω-cm ²)
520 °C	0.0693	0.087	0.214
470 °C	0.219	0.101	0.405
420 °C	0.227	0.363	1.19
BZY/SFT/BZY under H₂/Air			
520 °C	0.1203	0.1	0.639
470 °C	0.221	0.143	0.807
420 °C	0.37	0.34	1.23
SFT under 5% H₂ 95%Ar			
520 °C	0.11	0.09	0.895
470 °C	0.13	0.147	1.311
420 °C	0.153	0.35	1.4

devices [16,17,29]. The proton conductor usually needed lower activation energy than the oxide ions conduction, which benefitted from high ionic conductivity. Such high ionic conduction is due to surface doping, core-shell structure, low grain boundary resistance, and the Schottky junction. Also, such appreciable ionic

conductivity, especially the protons conduction, might play a crucial role in emerging semiconductor-based low-temperature fuel cells.

3.3. Electrochemical fuel cell performance

The I–V/I–P characteristics curve of SFT have been performed under the H₂/Air environments at different operational temperature 420–520 °C are shown in below Fig. 4 (a, b). The prepared device Ni/NCAL/SFT/NCAL/Ni displayed a pretty attractive power density of 534 mW/cm² and a higher OCV 1.04 V at 520 °C. Besides, the cell showed a power-output of 430 mW/cm², 350 mW/cm² at 470 and 420 °C, and a higher OCV of 1.05 V and 1.06 V, respectively, following the Nernst potential. Many factors influence such high performance at low operational temperature, including surface doping, which causes more O-vacancies to enhance the ionic conductivity. The core-shell structure is another factor for the easy transportation of ions, primarily protons, through the amorphous phase at the surface. Moreover, the lower value of grain boundary resistance assists in fast transportation of charges, enhancing the ionic conductivity of prepared SFT lattice [17]. Also, due to the amphoteric semiconducting nature of SFT, the existence of the

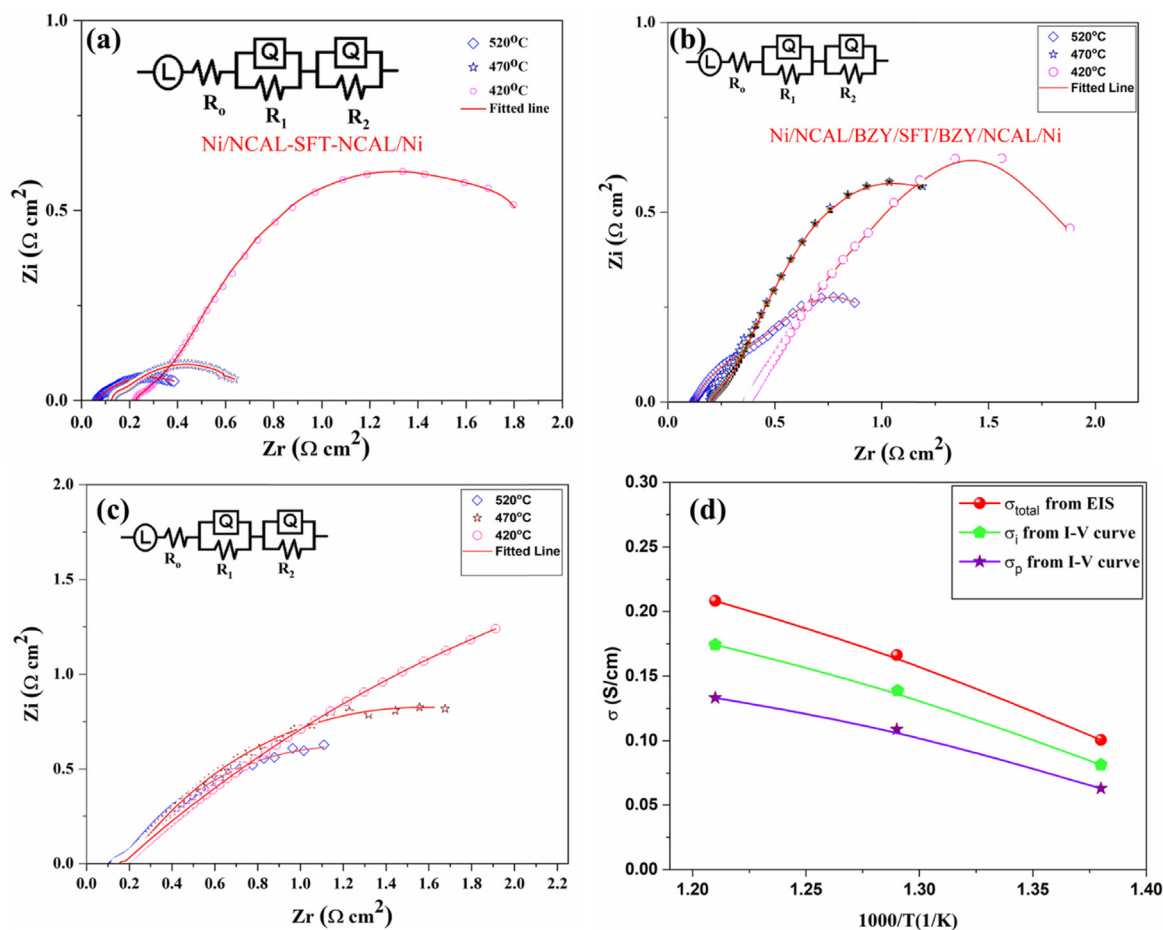


Fig. 3. (a–c) EIS analysis of SFT (a) Ni/NCAL-SFT-NCAL/Ni, (b) Ni/NCAL/BZY-SFT-BZY/NCAL/Ni under H_2/Air environment and (c) Ni/NCAL-SFT-NCAL/Ni under H_2 and 5% H_2 95%Ar at different operational temperature 420–520 °C, while (d) reveals the total, ionic and protonic conductivity at 420–520 °C.

Schottky junction play a crucial role in suppressing the electronic conduction and act as a driving force to excel the ions' transportation through the electrolyte layer [31–33]. Additionally, the fuel cell cross-sectional image of Ni/NCAL/SFT/NCAL/Ni has been displayed in Fig. 4(c). It should be noticed the electrolyte membrane SFT is well compacted or sandwiched between two symmetrical electrodes, and electrodes seem to be much porous, which guarantees high ionic of electrolyte and better catalytic activity of Ni-NCAL electrodes in the prepared device of SOFC [25].

Furthermore, electrical properties reveal that the prepared SFT semiconductor owns underlying proton-conduction and a high level of ionic conductivity at 420–520 °C. Therefore, the following configuration Ni-NCAL/BZY/SFT/BZY/NCAL/Ni of a blocking fuel cell was fabricated to verify the proton conduction using the proton conductor BZY as a blocking layer or filtering layer [29]. To measure the specific ionic conductivity, a cell with a blocking approach was adopted in past literature to eliminate the impact of other charge carriers [29]. The I–V curve has been tested the same way as above; moreover, BZY is purely a proton conductor, so it only lets H^+ pass through the membrane while blocking the other carriers (O^{2-}/e^-). The maximum power output of 474 mW/cm^2 has been achieved which, is about 90% of total fuel cell performance (without BZY layer 534 mW/cm^2) at 520 °C. The difference of 10% (loss in power-output) might be caused due to BZY own resistance and limited proton conductivity, and more polarization losses due to additional interfaces.

Moreover, neither power nor the OCV loss has been noticed in both cases, which confirms no electrons passageway over the electrolyte layer to cause the short-circuiting of the device. Also, using the BZY blocking layer ensures no contribution of electrons conduction to overall conductivity. Fig. 4(d) shows the SEM cross-sectional image of the blocking cell or five-layer device. The blocking cell contains five layers, including NCAL symmetrical electrodes, BZY blocking layer, and SFT electrolyte layer, undoubtedly distinguished in the obtained SEM image, suggesting the practical construction of a five-layer device or blocking cell (O^{2-}/e^-) [17,29]. Moreover, five-layer device performance and EIS under H_2/air environment have been repeated at 520 °C as shown in Fig. S1 (5, 6).

Moreover, the protonic cell was used to further study the fuel cell performance further and electrical properties using different intervals of time such as 0 h–90 h at 520 °C under H_2/air environments as depicted in below Fig. 5(a and b), respectively. The prepared cell in 0 h possesses peak power density 474 mW/cm^2 at 1.45 A/cm^2 , with an ohmic resistance R_0 of 0.1203 $\Omega\text{-cm}^2$ and polarization resistance R_p of 0.739 $\Omega\text{-cm}^2$. Afterward, a slight degradation in performance was noticed along with ohmic and polarization resistance; after 30 h, performance was 462 mW/cm^2 with ohmic and polarization resistance of 0.15 and 0.79 $\Omega\text{-cm}^2$. After 90 h, the performance of the prepared cell was 451 mW/cm^2 and ohmic and polarization resistance 0.21 and 1.07 $\Omega\text{-cm}^2$. After 90 h, the degradation in power and resistance was a little higher,

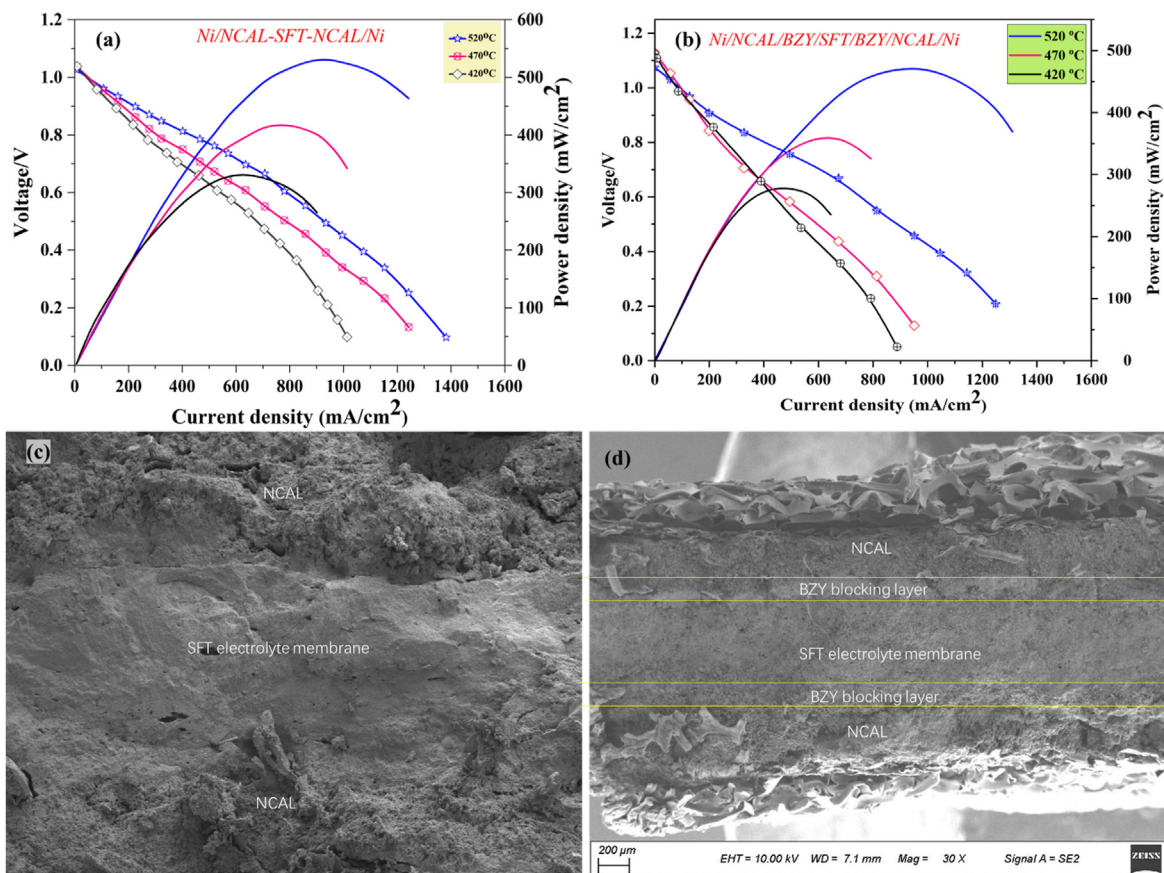


Fig. 4. (a–c) I/V characteristics curve of SFT (a) Ni/NCAL-SFT-NCAL/Ni, (b) Ni/NCAL/BZY-SFT-BZY/NCAL/Ni under H₂/Air environment at different operational temperature 520–420 °C, while (c, d) shows the cross-sectional view of Ni/NCAL-SFT-NCAL/Ni and Ni/NCAL/BZY-SFT-BZY/NCAL/Ni.

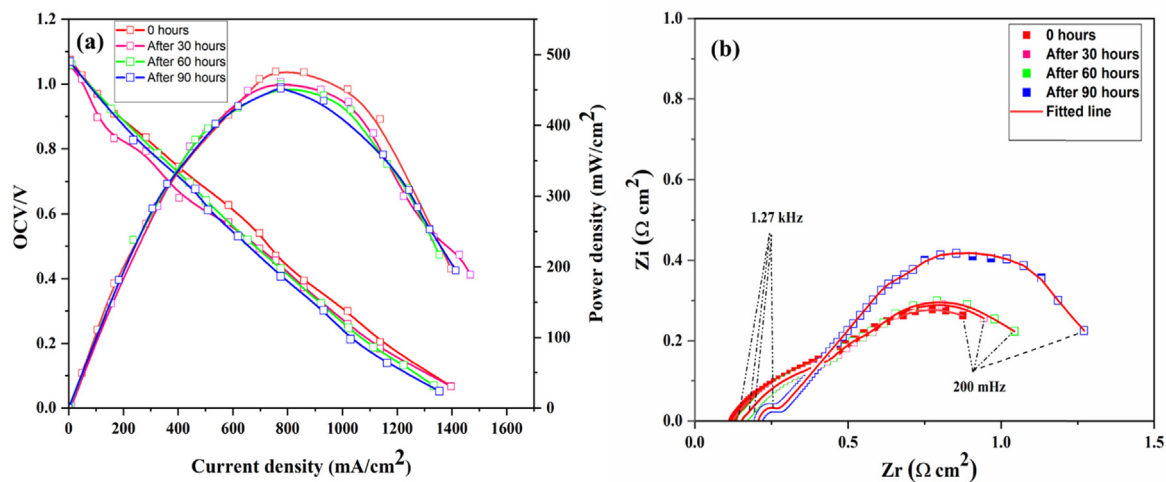


Fig. 5. (a, b) Fuel cell performance and EIS analysis of Ni/NCAL/BZY-SFT-BZY/NCAL/Ni under H₂/Air environment with different intervals.

which might happen due to some chemical reaction or high polarization losses with time. Still, overall, the performance was stable, and resistance was relatively low, which benefits the promotion of ions in the prepared lattice. The detailed inspection of EIS and fuel cell performance with different intervals have been presented separately in the supplementary information (Fig S17,8 (a–d)). The EIS and fuel cell performance suggest that the prepared device with surface doping can significantly improve the

proton conduction (grain-boundary and bulk conduction), which guarantees better fuel cell performance at a low operating temperature of 520 °C.

3.4. XPS spectra

Additionally, an XPS study was executed to investigate the surface properties of prepared electrolyte materials. The XPS full

spectrum of SFT constitutes all elements, including Sr-3d, Fe-2p, Ti-2p and O-1s, as displayed in SI Fig. 3. The prominent peak of Sr-3d located at 133 eV and 134 eV are linked to Sr-3d_{5/2} and Sr-3d_{3/2}, respectively, as visualized in Fig. 6(a). The peaks of Fe mainly reside at different binding energy 709.8 eV and 722.8 eV concerned to the Fe-2p_{3/2} and Fe-2p_{1/2}. The Fe peaks are further divided into six more peaks, including two peaks of Fe⁺³ and satellite peaks located at 710.0, 723.20 and 714.53 eV. An additional two peaks of Fe⁺² is observed at 708.50 and 722.00 eV, with satellites peaks at 729.89 eV. The XPS spectrum consists of four characteristics sub-peaks of Ti 2p. The sub-peaks are positioned at 458.03 and 463.85 eV with Ti⁺⁴, as shown in Fig. 6(c). The difference of 5.82 eV can be noticed between Ti⁺⁴-2p_{3/2} and Ti⁺⁴-2p_{1/2}, which is larger than the theoretical value of Ti (5.74 eV), leading to Fe's being well incorporated into STO, especially in Ti through surface doping [34,35]. Also, the sub-peaks of Ti⁺³-2p_{3/2} and Ti⁺³-2p_{1/2} situated at 459.43 eV and 465.33 eV resemble Ti atoms of TiO₂, which is bounded to O.

Furthermore, Fig. 6 (d) shows the spectra of O-1s with three different peaks positioned at 529.2 eV and 531.3 eV are allotted to lattice-oxide and hydroxyl groups leading to enhance the surface hydroxyl group and enhancing the proton transportation. The peak at 531.8 eV in SFT is tentatively assigned to oxide ions bonded to Fe⁺³ ions near the surface of a lattice. Also, compared to STO, the SFT O peak shift toward lower binding energy might be attributed to a change in charge distribution. This causes to enlarge the O-

vacancies, which results in enhanced ionic conductivity, especially the protons conductivity [36,37]. Moreover, the peak area has been expanded upon doping, resembling the creation of more O-vacancies and high ionic conduction channels [35,37].

3.5. Schottky-junction, and durability of fuel cell

The produced electrons at the (anode/electrolyte) interface in fuel cell mode must follow the desired direction through an external circuit to make the electric current. However, if it follows the path through the electrolyte layer, it causes degradation in fuel cell performance and OCV. Therefore, to prevent the passage of electrons through electrolytes, Schottky junction phenomena have been proposed and performed as demonstrated in Fig. 7(a) [38]. In the Schottky junction fuel cell device, a potential can be developed at the established interface of metal & semiconductors either p-type or n-type. However, SFT is a p-type semiconductor, and produced potential between metal and semiconductor is also termed a Schottky barrier [32]. In fuel cell mode at the anode side, H₂ injection causes a reduction of the anode NCAL into Ni/Co metal which forms the Schottky junction with the SFT semiconductor, as shown in Fig. 7(a). The formation of the Schottky junction cause to produces a depletion layer at the interface, which further constitutes a build in the potential whose direction is from the metal side to towards semiconductor [38]. BIEF and Schottky barriers were formed in the fuel cell device to stop the electronic movement

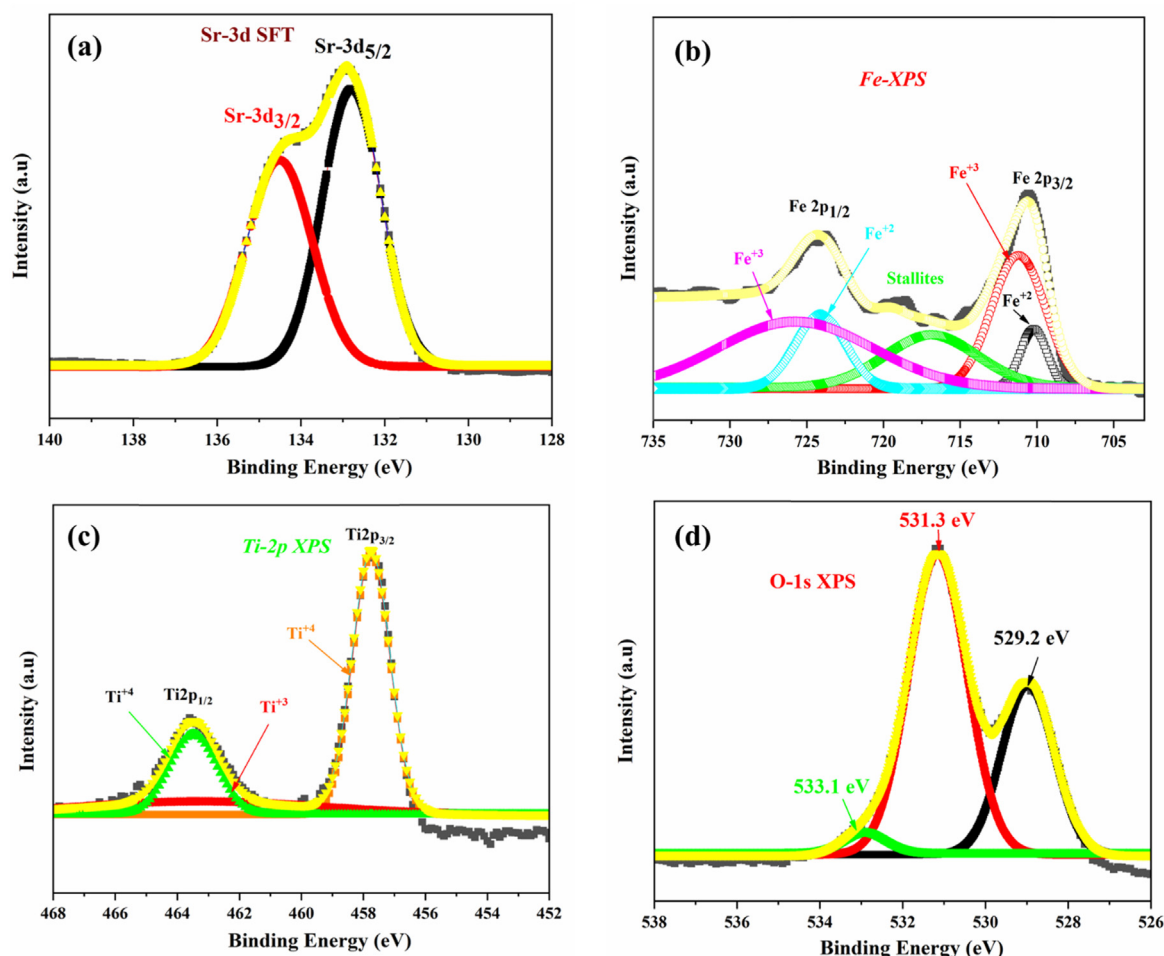


Fig. 6. (a–d) XPS analysis of SFT with all elements including (a) Sr-3d, (b) Fe-2p, (c) Ti-2p and (d) O-1s.

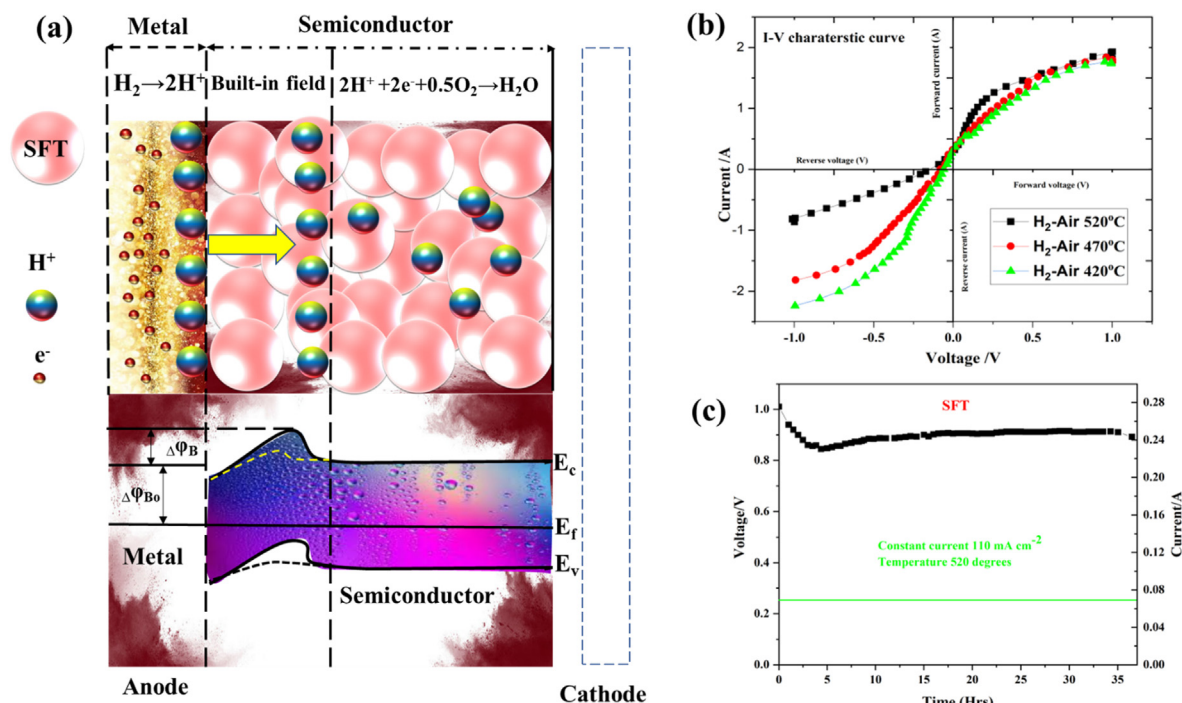


Fig. 7. (a) The mechanism of Schottky junction between metal and semiconductor Ni/Co/SFT, (b) exhibit the I–V characteristic curve under H₂/Air environment at different operational temperature 520–420 °C, (c) durability operation of SFT electrolyte with constant current 110 mA cm⁻² at 520 °C.

through the electrolyte and force it through an external circuit to produce an electric current.

Meanwhile, BIEF works as a secondary driving force to boost the ionic conduction through the lattice. Furthermore, to approve the presence of Schottky junction, (I–V) characteristics curve of the following cell (Ni-NCAL/SFT) has been tested at different operating temperatures as displayed in Fig. 7(b) [32]. The current response of the prepared half-cell was noted by setting the bias-voltage from -1 to 1 V at different operational temperatures (420–520 °C). Before supplying H₂ at the anode side, no junction effect has been observed at the interface (anode & semiconductor electrolyte). The rectification behavior of (I–V) was noticed as H₂ was inserted to the anode side. Under the reverse bias voltage (–1–0 V), the device shows little saturation in the current response. According to the Schottky equation $I = I_s(e^{\frac{eV_A}{kT}} - 1)$, the current of the prepared device increased rapidly under a higher bias voltage. The parameters of above stated equation have been described elsewhere [39]. The presented results verify the formation of the Schottky-junction (SJ) among the reduced NCAL (metallic-phase) anode and semiconductor SFT electrolyte [32,38].

The durability operation of SFT electrolyte-based fuel cell has been performed at 520 °C in fuel-cell working conditions, as demonstrated in Fig. 7 (c). The prepared cell stays stable for almost 36 h at the OCV of 0.84 V with a higher and stable current density of 110 mA/cm⁻² under different gas environments H₂/Air. Before reaching the stable point at the initial stage, the OCV decreased slowly and smoothly for almost 5 h. Then without any degradation, it came to a steady level of 0.84 V. The operational stability primarily owes to the surface doping of Fe and the formation of the Schottky junction. It also supports the feasibility of SFT as an electrolyte. The initial process of falling in stability might appear due to a delay in the activation of electrodes. Then, as it got activated, protons insertion in the SFT lattice caused to enhance the voltage to a stable level, leading to improved proton conduction.

Also, the interface gap might be the reason for the initial-activation process leading to a bit of drop in OCV until the gap was bridged with the ions channels to continue the cell operation. Besides, the densification of the electrolyte layer might be the possible reason for the dropping of OCV at the start. The electrolyte layer was not so dense and could cause gas leakage, but with online densification, the voltage gets stable. Advanced engineering technology is urgently mandatory to extend the stability for a longer time.

4. Conclusion

A single-phase SFT with surface doping was synthesized here using a sol-gel method for use as a LT-FC electrolyte application. Material characterization such as the XRD, SEM, TEM, and XPS verified the desirable single-phase structure of SFT was obtained with pure phase, functional morphology and enriched oxygen vacancy concentration due to surface doping of Fe into STO lattice. The developed SFT electrolyte exhibited the most competent and reliable fuel cells functionality. The prepared fuel cell delivered an output 534 mW/cm² and high ionic conductivity 0.18 S/cm at 520 °C. Furthermore, the five-layer device of Ni/NCAL/BZY-SFT-BZY/NCAL/Ni has exhibited an outstanding performance output of 474 mW/cm² along with high proton conduction of 0.14 S/cm. EIS results of three cells with different environments reveal that the small grain-boundary and electrode polarization resistances of SFT played an essential role in high performance. Also, the EIS and fuel cell performance of Ni/NCAL/BZY-SFT-BZY/NCAL/Ni with different intervals have been evaluated, leading to the fact that neither the performance drop nor the resistance increases with time. To interpret the high OCVs and power outputs, the Schottky junction phenomena presented along with the I–V curve at a different temperature helps subtract electronic conduction through fuel cell devices. The BIEF at the junction helps block the electronic conduction and helps in excelling the ionic, especially the proton

transport through the electrolyte layer. The presented semiconductor membrane has provided us with new functionalities and design available materials that can be used as a functional electrolytes for advanced low-temperature ceramic fuel cells.

Declaration of competent interest

We do not have any competing financial interests or personal relationships that influence current work's reported paper.

CRediT authorship contribution statement

M.A.K. Yousaf Shah: Formal analysis, Writing – original draft, carried out synthesis, characterizations, paper write, participated in device optimization and data analysis, verified fuel cell results, wrote the paper. **Yuzheng Lu:** Conceptualization, Formal analysis, the idea, designed the experiments, and analyzed the data. **Naveed Mushtaq:** Formal analysis, carried out few characterizations and device optimizations, participated in device optimization and data analysis. **Sajid Rauf:** Formal analysis, participated in device optimization and data analysis. **Muhammad Yousaf:** Formal analysis, Writing – review & editing, revised some parts of the manuscript and performed a stability test, analyzed the X.R.D results. **Muhammad Imran Asghar:** Formal analysis, Writing – original draft, participated in device optimization and data analysis, wrote the paper. **Peter D. Lund:** Formal analysis, Writing – original draft, participated in device optimization and data analysis, wrote the paper. **Bin Zhu:** Conceptualization, Formal analysis, Writing – original draft, the idea, designed the experiments, and analyzed the data, participated in device optimization and data analysis, wrote the paper. All authors commented on the manuscript.

Declaration of competing interest

The authors declare that they have no known competing financial interests or personal relationships that could have appeared to influence the work reported in this paper.

Acknowledgement

This work was supported Southeast University (SEU) project 3203002003A1 and National Natural Science Foundation of China (NSFC) under the grant 51772080 and 11604088. Jiangsu Provincial Innovation and Entrepreneurship Talent program Project No. JSSCRC2021491. Industry-University-Research Cooperation Project of Jiangsu Province in China, Grant No. BY2021057. Dr. Asghar thanks the Hubei Talent 100 program and Academy of Finland (13329016, 13322738) for their financial support.

Appendix A. Supplementary data

Supplementary data related to this article can be found at <https://doi.org/10.1016/j.renene.2022.06.154>.

References

- [1] E.P. Murray, T. Tsai, S.A. Barnett, A direct-methane fuel cell with a ceria-based anode, *Nature* 400 (6745) (1999 Aug) 649–651.
- [2] S. Park, J.M. Vohs, R.J. Gorte, Direct oxidation of hydrocarbons in a solid-oxide fuel cell, *Nature* 404 (6775) (2000 Mar) 265–267.
- [3] T. Hibino, A. Hashimoto, T. Inoue, J.I. Tokuno, S.I. Yoshida, M. Sano, A low-operating-temperature solid oxide fuel cell in hydrocarbon-air mixtures, *Science* 288 (5473) (2000 Jun 16) 2031–2033.
- [4] T.A. Adams, J. Nease, D. Tucker, P.I. Barton, Energy conversion with solid oxide fuel cell systems: a review of concepts and outlooks for the short-and long-term, *Ind. Eng. Chem. Res.* 52 (9) (2013 Mar 6) 3089–3111.
- [5] P.I. Cowin, C.T. Petit, R. Lan, J.T. Irvine, S. Tao, Recent progress in the development of anode materials for solid oxide fuel cells, *Adv. Energy Mater.* 1 (3) (2011 May) 314–332.
- [6] A.J. Jacobson, Materials for solid oxide fuel cells, *Chem. Mater.* 22 (3) (2010 Feb 9) 660–674.
- [7] S. Choi, S. Yoo, J. Kim, S. Park, A. Jun, S. Sengodan, J. Kim, J. Shin, H.Y. Jeong, Y. Choi, G. Kim, Highly efficient and robust cathode materials for low-temperature solid oxide fuel cells: PrBa 0.5 Sr 0.5 Co 2– x Fe x O 5– δ , *Sci. Rep.* 3 (1) (2013 Aug 15) 1–6.
- [8] J.G. Lee, J.H. Park, Y.G. Shul, Tailoring gadolinium-doped ceria-based solid oxide fuel cells to achieve 2 W cm^{–2} at 550 C, *Nat. Commun.* 5 (1) (2014 Jun 4), 1–0.
- [9] Y. Yamazaki, R. Hernandez-Sanchez, S.M. Haile, High total proton conductivity in large-grained yttrium-doped barium zirconate, *Chem. Mater.* 21 (13) (2009 Jul 14) 2755–2762.
- [10] J. Tong, D. Clark, M. Hoban, R. O'Hayre, Cost-effective solid-state reactive sintering method for high conductivity proton conducting yttrium-doped barium zirconium ceramics, *Solid State Ionics* 181 (11–12) (2010 Apr 29) 496–503.
- [11] D. Pergolesi, E. Fabbri, A. D'Epifanio, E. Di Bartolomeo, A. Tebano, S. Sanna, S. Licocchia, G. Balestrino, E. Traversa, High proton conduction in grain-boundary-free yttrium-doped barium zirconate films grown by pulsed laser deposition, *Nat. Mater.* 9 (10) (2010 Oct) 846–852.
- [12] P. Babilo, T. Uda, S.M. Haile, Processing of yttrium-doped barium zirconate for high proton conductivity, *J. Mater. Res.* 22 (5) (2007 May) 1322–1330.
- [13] P. Babilo, S.M. Haile, Enhanced sintering of yttrium-doped barium zirconate by addition of ZnO, *J. Am. Ceram. Soc.* 88 (9) (2005 Sep) 2362–2368.
- [14] K.D. Kreuer, Aspects of the formation and mobility of protonic charge carriers and the stability of perovskite-type oxides, *Solid State Ionics* 125 (1–4) (1999 Oct 1) 285–302.
- [15] K.D. Kreuer, W. Münch, A. Fuchs, U. Klock, J. Maier, Proton conducting alkaline earth zirconates and titanates for high drain electrochemical applications, *Solid State Ionics* 145 (1–4) (2001 Dec 1) 295–306.
- [16] Y. Zhou, X. Guan, H. Zhou, K. Ramadoss, S. Adam, H. Liu, S. Lee, J. Shi, M. Tsuchiya, D.D. Fong, S. Ramanathan, Strongly correlated perovskite fuel cells, *Nature* 534 (7606) (2016 Jun) 231–234.
- [17] Y. Xing, Y. Wu, L. Li, Q. Shi, J. Shi, S. Yun, M. Akbar, B. Wang, J.S. Kim, B. Zhu, Proton shuttles in CeO₂/CeO₂– δ core–shell structure, *ACS Energy Lett.* 4 (11) (2019 Oct 3) 2601–2607.
- [18] E.C. Souza, R. Muccillo, Properties and applications of perovskite proton conductors, *Mater. Res.* 13 (2010) 385–394.
- [19] K. Katahira, Y. Kohchi, T. Shimura, H. Iwahara, Protonic conduction in Zr-substituted BaCeO₃, *Solid State Ionics* 138 (1–2) (2000 Dec 1) 91–98.
- [20] F. Iguchi, N. Sata, T. Tsurui, H. Yugami, Microstructures and grain boundary conductivity of BaZr_{1–x}Y_xO₃ (x= 0.05, 0.10, 0.15) ceramics, *Solid State Ionics* 178 (7–10) (2007 Apr 1) 691–695.
- [21] S. Barison, M. Battagliarin, T. Cavallin, S. Daolio, L. Doubova, M. Fabrizio, C. Mortalò, S. Boldrini, R. Gerbasi, Barium non-stoichiometry role on the properties of Ba_{1+x}CeO₃, *Solid State Ionics* 150(3–5) (2002) 360–368.
- [22] B. Zhu, S. Yun, P.D. Lund, Semiconductor-ionic materials could play an important role in advanced fuel-to-electricity conversion, *Int. J. Energy Res.* 42 (2018) 3413–3415.
- [23] G. Chen, Y. Luo, W. Sun, H. Liu, Y. Ding, Y. Li, S. Geng, K. Yu, G. Liu, Electrochemical performance of a new structured low temperature SOFC with BZY electrolyte, *Int. J. Hydrogen Energy* 43 (28) (2018 Jul 12) 12765–12772.
- [24] M.Y. Shah, S. Rauf, N. Mushtaq, Z. Tayyab, N. Ali, M. Yousaf, Y. Xing, M. Akbar, P.D. Lund, C.P. Yang, B. Zhu, Semiconductor Fe-doped SrTiO₃– δ perovskite electrolyte for low-temperature solid oxide fuel cell (LT-SOFC) operating below 520° C, *Int. J. Hydrogen Energy* 45 (28) (2020 May 21) 14470–14479.
- [25] M.A. Shah, N. Mushtaq, S. Rauf, C. Xia, B. Zhu, The semiconductor SrFeO₃. 2TiO₃. 8O₃– δ -ZnO heterostructure electrolyte fuel cells, *Int. J. Hydrogen Energy* 44 (57) (2019 Nov 15) 30319–30327.
- [26] X. Chen, S. Zhan, D. Chen, C. He, S. Tian, Y. Xiong, Grey Fe-CeO₂- σ for boosting photocatalytic ozonation of refractory pollutants: roles of surface and bulk oxygen vacancies, *Appl. Catal. B Environ.* 286 (2021 Jun 5), 119928.
- [27] S. Rauf, B. Zhu, M.Y. Shah, C. Xia, Z. Tayyab, N. Ali, C. Yang, N. Mushtaq, M.I. Asghar, F. Akram, P.D. Lund, Tailoring triple charge conduction in BaCo_{0.2}Fe_{0.1}Ce_{0.2}Tm_{0.1}Zr_{0.3}Y_{0.1}O₃– δ semiconductor electrolyte for boosting solid oxide fuel cell performance, *Renew. Energy* 172 (2021 Jul 1) 336–349.
- [28] N. Mushtaq, C. Xia, W. Dong, G. Abbas, R. Raza, A. Ali, S. Rauf, B. Wang, J.S. Kim, B. Zhu, Perovskite SrFe_{1-x}Ti_xO₃– δ (x<= 0.1) cathode for low temperature solid oxide fuel cell, *Ceram. Int.* 44 (9) (2018 Jun 15) 10266–10272.
- [29] C. Xia, Y. Mi, B. Wang, B. Lin, G. Chen, B. Zhu, Shaping triple-conducting semiconductor BaCo 0.4 Fe 0.4 Zr 0.1 Y 0.1 O 3– δ into an electrolyte for low-temperature solid oxide fuel cells, *Nat. Commun.* 10 (1) (2019 Apr 12) 1–9.
- [30] B. Zhu, L. Fan, N. Mushtaq, R. Raza, M. Sajid, Y. Wu, W. Lin, J.S. Kim, P.D. Lund, S. Yun, Semiconductor electrochemistry for clean energy conversion and storage, *Electrochem. Energy Rev.* 25 (2021 Oct) 1–36.
- [31] C. Xia, Z. Qiao, L. Shen, X. Liu, Y. Cai, Y. Xu, J. Qiao, H. Wang, Semiconductor electrolyte for low-operating-temperature solid oxide fuel cell: Li-doped ZnO, *Int. J. Hydrogen Energy* 43 (28) (2018 Jul 12) 12825–12834.
- [32] B. Zhu, P.D. Lund, R. Raza, Y. Ma, L. Fan, M. Afzal, J. Patakangas, Y. He, Y. Zhao, W. Tan, Q.A. Huang, Schottky junction effect on high performance fuel cells based on nanocomposite materials, *Adv. Energy Mater.* 5 (8) (2015 Apr),

- 1401895.
- [33] E. Hu, Z. Jiang, L. Fan, M. Singh, F. Wang, R. Raza, M. Sajid, J. Wang, J.S. Kim, B. Zhu, Junction and energy band on novel semiconductor-based fuel cells, *iScience* 12 (2021 Feb), 102191.
- [34] K. Lankauf, A. Mrozinski, P. Biaszcak, K. Górnicka, J. Ignaczak, M. Łapinski, et al., The effect of Fe on chemical stability and oxygen evolution performance of high surface area SrTix-1FexO3-d mixed ionic-electronic conductors in alkaline media, *Int. J. Hydrogen Energy* 46 (2021) (28575), e28590.
- [35] N. Mushtaq, C. Xia, W. Dong, B. Wang, R. Raza, A. Ali, et al., Tuning the energy band structure at interfaces of the SrFe0.75Ti0.25O3-δ-Sm0.25Ce0.75O2-δ heterostructure for fast ionic transport, *ACS Appl. Mater. Interfaces* 11 (42) (2019) 38737–38745.
- [36] W. Dong, Y. Tong, B. Zhu, H. Xiao, L. Wei, C. Huang, et al., Semiconductor TiO₂ thin film as an electrolyte for fuel cells, *J. Mater. Chem.* 7 (28) (2019) 16728–16734.
- [37] M.Y. Shah, B. Zhu, S. Rauf, N. Mushtaq, M. Yousaf, N. Ali, et al., Electrochemical properties of a co-doped SrSnO₃-δ-based semiconductor as an electrolyte for solid oxide fuel cells, *ACS Appl. Energy Mater.* 3 (7) (2020) 6323–6333.
- [38] M.Y. Shah, S. Rauf, N. Mushtaq, B. Zhu, Z. Tayyab, M. Yousaf, et al., Novel perovskite semiconductor based on Co/Fe-codoped LBZY (La_{0.5}Ba_{0.5}Co_{0.2}Fe_{0.2}Zr_{0.3}O_{3-δ}) as an electrolyte in ceramic fuel cells, *ACS Appl. Energy Mater.* 4 (6) (2001) 5798–5808.
- [39] J. Lutz, H. Schlagenotto, U. Scheuermann, R. De Doncker, Semiconductor power devices, *Phys. Charact. Reliabil.* 2 (2011).